

High fidelity single-pixel imaging

CHAO DENG^{1,2}, XUEMEI HU³, XIAOXU LI¹, JINLI SUO¹, ZHILI ZHANG², AND QIONGHAI DAI¹

¹Department of Automation, Tsinghua University, Beijing, 100084, China

²High-Tech Institute of Xi'an, Xi'an, 710025, China

³School of Electronic Science and Engineering, Nanjing University, Nanjing, 210000, China

Compiled July 10, 2021

Single-pixel imaging (SPI) is an emerging technique which has attracts wide attention in various research fields. However, restricted by the low reconstruction quality and large amount of measurements, the practical application is still in its infancy. Inspired by the fact that natural scenes exhibit unique degenerate structures in the low dimensional subspace, we propose to take advantage of the local prior in convolutional sparse coding to implement high fidelity single-pixel imaging. Specifically, by statistically learning strategy, the target scene can be sparse represented on an over-complete dictionary. The dictionary is composed of various basis learned from a natural image database. We introduce the above local prior into conventional SPI framework to promote the final reconstruction quality. Experiments both on synthetic data and real captured data demonstrate that our method can achieve better reconstruction from the same measurements, and thus consequently reduce the number of required measurements for same reconstruction quality. © 2021 Optical Society of America

<http://dx.doi.org/10.1364/ao.XX.XXXXXX>

1. INTRODUCTION

Single-pixel imaging (SPI) is a novel imaging scheme which correlates two beams non-locally. These two light beams travel differently: one beam interacts with object and is recorded by a bucket detector, the other is directly collected by a spatially resolved detector. The object can be reconstructed by correlating the output of these two beams. At the beginning, SPI was considered as the unique mechanism of quantum entangle photons [1], which was referred as ghost imaging (GI). Soon after, classic thermal light was also proved to be successful under the same configuration [2–4]. Programmable illumination makes SPI more flexible and ready to put into practical applications, such as fluorescence imaging [5], remote sensing [6], 3D reconstruction [7], optical encryption [8, 9], and object tracking [10, 11].

So far, three typical categories of reconstruction algorithms for SPI has been proposed: linear correlation method [12–15], the alternating projection (AP) method [16–18] and compressive sensing (CS) based method [19, 20]. The correlation-based meth-

ods restore the specific object through second order or higher order correlations, which suffer from low reconstruction quality and large amount of measurements. The AP algorithm incorporates the constraints from the patterned illumination and correlated measurements in spatial and Fourier domain alternatively. It typically iterates 100 ~ 200 rounds (each round includes all the iteration over each measurement) until the final convergence. In contrast, the compressed sensing-based methods are more efficient which need far lower measurements with faster convergence compared with the former two.

The compressed sensing algorithm in SPI introduces the image priors into the under-determined linear system to decrease the solution space. Two widely used priors are sparse representation prior and the total variation (TV) regularization prior [21]. The former states that natural images can be sparse represented in some orthogonal basis as DCT and wavelet [22, 23], and the latter considers the gradient integral as statistically low. Such global priors constraint all the natural images from the general perspective and improve the final reconstruction. Except for global prior, the natural images of specific class exhibit unique degenerate structure, which can be sparse denoted in the low-dimensional self-characteristic subspace. For example, image statistics suggest that the image patches can be well represented on an over-complete dictionary [24–27], which is termed as the sparse coding (SC). Local prior as such in sparse coding has been widely used and achieved state-of-the-art performances in computer vision, such as denoising, deblurring, inpainting, super resolution imaging and machine learning.

Sparse coding aims to construct an over-complete dictionary in which a sparse linear combination of atoms can well approximate the original image. The atoms of over-complete dictionary are intrinsic structures learned from thousands of images. Patch-based SC considers overlapped patches as sub-elements and processes them separately. Each patch can be sparse represented and the whole image is reconstructed by the average of these patches. Although the patch-based method can reduce the calculation size in optimization and achieve high-quality representation, two limitations arising in this method suppress the final reconstruction in various task. First, since the simple variance of intrinsic structure (such as shift or rotation) is indistinguishable due to the independent mechanism in patch-based SC, the learned dictionary is highly redundant. Second, the overlap-averaging mechanism leads to the inconsistency of overlapped patches [28]. As opposed to the patched-based SC, the convolutional sparse coding (CSC) decomposes the whole image

into some sparse feature maps thus avoid the prior consistency of learned atoms and inconsistency of overlapped patches. The CSC can model the image more explicitly than patched-based SC through convolution operator.

In this paper, we propose to incorporate the local prior in convolutional sparse coding with the global prior to implement high fidelity single-pixel imaging. Our framework can greatly improve the reconstruction in non-spatially resolved imaging technique compared with current state-of-the-art methods, and have further promotion in practical application. The remaining part of the paper is organized as follows: In section 2, we introduce our modeling and derivative process mathematically. In Section 3, we evaluate the performance of our method both on simulation and experiment. Finally in section 4, we summarise the disadvantages and limitations of our work.

2. METHOD

To fully exploit the image prior both globally and locally, we incorporate these two priors together for high fidelity reconstruction. Mathematically, we can learn the kernels of CSC from large numbers of nature images by the following optimization [29, 30]

$$\begin{aligned} \arg \min_{\mathbf{d}, \mathbf{s}} \quad & \sum_{j=1}^J \frac{1}{2} \|\mathbf{x}^j - \sum_{k=1}^K \mathbf{d}_k * \mathbf{s}_k^j\|_2^2 + \beta \sum_{k=1}^K \|\mathbf{s}_k^j\|_1 \\ \text{s.t.} \quad & \|\mathbf{d}_k\|_2^2 \leq 1 \quad \forall k \in \{1, \dots, K\}, \end{aligned} \quad (1)$$

where each image \mathbf{x}^j can be represented as the summation of vectorized 2D kernels \mathbf{d}_k convolved with corresponding sparse feature maps \mathbf{s}_k^j . Here \mathbf{x}^j and \mathbf{s}_k^j are both vectorized form. β weights the ℓ_1 penalty, and we set $\beta = 1$ for its good tradeoff between sparsity and data fitting as in [30]. The operation $*$ denotes the 2D convolution defined on the vectorized inputs. We use the fast and flexible algorithm proposed in [30] to obtain the over-complete dictionary of convolve sparse coding.

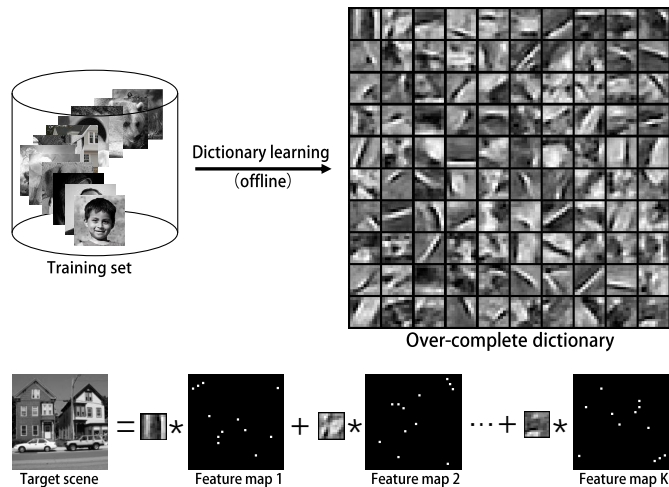


Fig. 1. The overview of our model. The upper part describes the learning process of convolutional sparse coding. With the learned dictionary, the target scene can be decomposed as summation of kernels convolved with corresponding sparse feature maps.

After the kernel learning as shown in Fig. 1, the over-complete dictionary can be utilized to decomposed the target

image. Introducing this local prior into SPI reconstruction, the optimization can be modeled as

$$\begin{aligned} \arg \min_{\mathbf{s}_k} \quad & \|\Psi \mathbf{x}\|_1 + \lambda \sum_{k=1}^K \|\mathbf{s}_k\|_1 \\ \text{s.t.} \quad & \mathbf{y} = \Phi \mathbf{x} \\ & \mathbf{x} = \sum_{k=1}^K \mathbf{s}_k * \mathbf{d}_k. \end{aligned} \quad (2)$$

Here Ψ is the transformation matrix of desired domain as DCT or TV, Φ is the sampling matrix with each row denoting the vectorized illumination pattern, \mathbf{y} is the single pixel measurement and λ is the penalty parameter. The first term in the objective function is the global constraint defined in the DCT or TV domain, and the second term local constraint on the learned dictionary.

For simplicity, we remove the intermediate variable \mathbf{x} and make the simple substitutions in Eq. 2, it can be rewritten as

$$\begin{aligned} \arg \min_{\mathbf{s}_k} \quad & \|\mathbf{v}\|_1 + \lambda \sum_{k=1}^K \|\mathbf{s}_k\|_1 \\ \text{s.t.} \quad & \mathbf{y} = \Phi \cdot \sum_{k=1}^K \mathbf{u}_k \\ & \mathbf{v} = \Psi \cdot \sum_{k=1}^K \mathbf{u}_k \\ & \mathbf{u}_k = \mathbf{s}_k * \mathbf{d}_k. \end{aligned} \quad (3)$$

We solve above optimization by alternating direction method of multipliers (ADMM) algorithm [31], and the target scene \mathbf{x} can be obtained by optimum \mathbf{s}_k^* . As for convolution operator in Eq. (3), we first transform \mathbf{s}_k and \mathbf{d}_k into respective Fourier space, and then implement Hadamard product. After Hadamard product in Fourier space, we inverse transform back to spatial domain. These calculation is faster than convolution operator since Fourier transform and Hadamard product are both simple matrix multiplication.

3. EXPERIMENTS ON SYNTHETIC DATA

To evaluate the performance of our method, we implement a series of simulations on the synthetic data. We first learn the over-complete dictionary of CSC by 20 randomly chosen images from the dataset built by the Stanford Vision Lab [32]. To balance the computational load and over-completeness, each kernel of the learned dictionary is set to 11×11 , and we have 100 kernels in total (The learned dictionary is shown in Fig. 1). We adopt the same dictionary size as in [30] to achieve good performance for general natural scenes. Then we conduct the CSC-based SPI framework using the ADMM optimization. The imaging size of target scene and modulation patterns are both 128×128 . All the test images are chosen out of training set. The measurement is generated by their inner product. We integrate CSC together with two aforementioned global priors as in TV and DCT domain, since these two constraints can achieve state-of-the-art performance in SPI.

To show the performance of CSC prior, we first conduct a simulation on several images under different compression ratio (i.e., pattern number divided by pixel number). We compare the reconstruction of two different groups: TV and TV+CSC, DCT and DCT+CSC, under the compression of 10%, 25%, 50% and 100%. The simulation result is shown in Fig. 2. The reconstruction using TV prior exhibits higher quality than DCT prior since

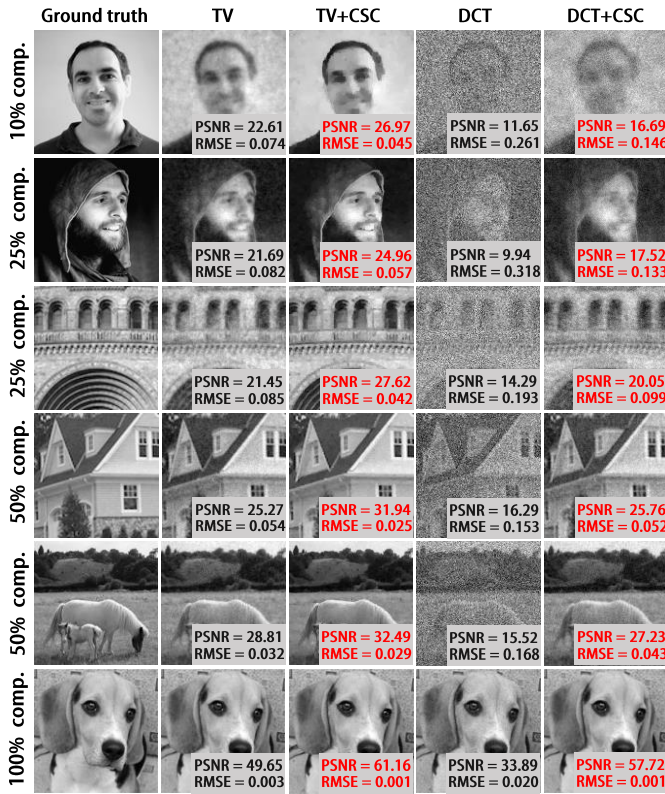


Fig. 2. The reconstruction comparison of four different combinations: TV, TV+CSC, DCT and DCT+CSC, under different compression ratio in terms of PSNR and RMSE.

all the test images are with non-periodic structures. In terms of peak-to-signal ratio (PSNR) and root mean square error (RMSE), the introduction of CSC prior can significantly improve the SPI reconstruction. Specifically, in this simulation, the promotion of PSNR is about 3.27 dB \sim 11.51 dB due to the CSC introduction into TV, and it turns 5.04 dB \sim 23.33 dB because of the CSC prior into DCT. Except for the PSNR, the improvement in RMSE is also significant. Different compression ratios and different images may vary in the promotion. The combination both globally and locally further reduces the solution space and improves the reconstruction accuracy.

For a better evaluation of the CSC prior, we investigate the average promotion on the image set under different compression ratio, which is ranging from 0.1 to 1.0 with the interval of 0.1. We choose 12 images from the database as the test set, which is composed of four different groups: person, animal, building and scenery, with 3 images in each group. We plot the average value and the extremum in Fig. 3. The simulation result suggests that the averaged improvement of CSC prior introduced into TV prior is about 2.5 \sim 6.4 dB (PSNR) and 0.011 \sim 0.044 (RMSE), while the promotion of CSC into DCT is 3.4 \sim 13.7 dB (PSNR) and 0.015 \sim 0.118 (RMSE). The advantage of introducing CSC is more distinct in DCT than TV. Larger compression ratio may be more likely to exhibit more marked PSNR promotion both in TV and DCT. The improvement of CSC introduction exhibit severe polarization on different images. The small value of minimum promotion curve close to 0 in PSNR and RMSE may caused by the untrained structure in training set. We can include more images into training set and increase the number of kernels to learn a more sufficient and effective over-complete dictionary.

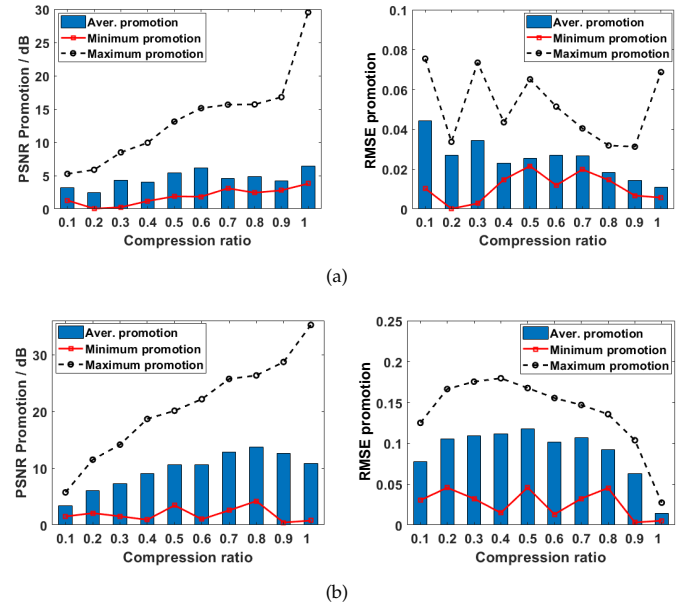


Fig. 3. Promotion of CSC introduced into TV (a) and DCT (b) in terms of PSNR and RMSE under different compression ratios.

In sum, the simulation result in Fig. 3 demonstrates that high fidelity image quality in SPI can achieved when we add the local prior of intrinsic structure into reconstruction.

The noise in the imaging process such as the sensor readout noise or intensity fluctuation of light source is inevitable in actual SPI experiment, so here we test the anti-noise capability of four aforementioned algorithms. We model the imaging noise as superimposing Gaussian white noise with the signal-to-noise ratio (SNR) ranging from 10 dB to 100 dB, and choose the RMSE as the evaluation metric. Without loss of generality, we specify the compression ratio as 0.25 in simulation. By comparing the RMSE scores of reconstruction under four different algorithms, the simulation results of two classic images "Lena" and "House" are shown in Fig. 4. Overall, the reconstruction of all the algorithms gets better as the noise level decreases, and becomes stable when the SNR exceeds 70 dB. As aforementioned, since the DCT algorithms prefer periodic structures, TV related methods have better performance than DCT related ones, especially under higher SNR. The gap before and after CSC introduction

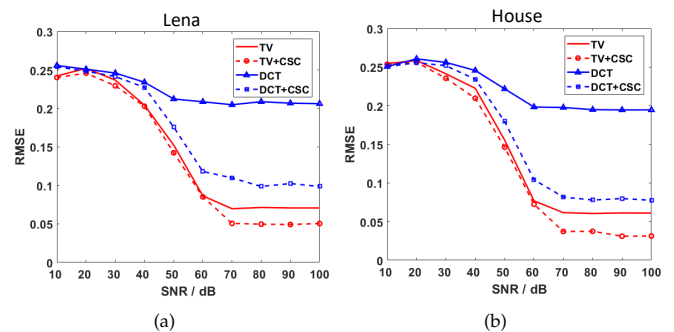


Fig. 4. The robust to imaging noise among four different algorithms of (a): "Lena" and (b): "House".

is increasing as the noise level decreases both in TV and DCT. This result guides us in actual experiment a lot: by minimising the imaging noise, we could achieve higher promotion through introducing additional CSC prior.

4. EXPERIMENTS ON REAL CAPTURED DATA

Finally, we experimentally demonstrate the performance of our method by the captured data of a prototype system. The scheme of our experimental setup is shown in Fig. 5. The light emitted from the halogen lamp is first collimated by a collimator composed of a condense lens, an optical integrator and a shaping lens. After collimation, a digital micromirror device (DMD) modulates the incoming light with random patterns. The outgoing light from the DMD is expanded by the projecting lens for scene illumination. After interaction with target scene, the outgoing photons are converged by a collecting lens and finally captured by a bucket detector.

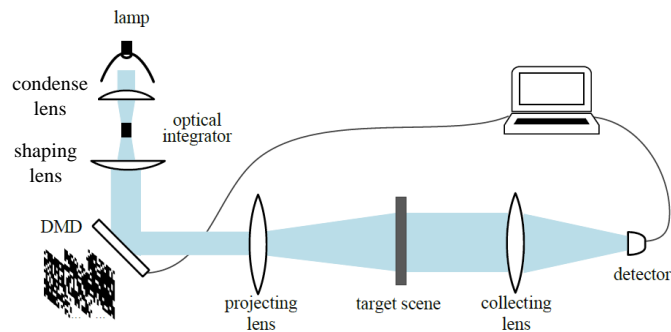


Fig. 5. The schematic diagram of our experimental setup. The high pressure Mercury lamp (Philips, 200w) is used as the light source. DMD: digital micromirror device (Texas Instrument DLP @DiscoveryTM4100, .7XGA). Detector: Thorlabs DET100 Silicon photodiode (integration time: 0.625ns).

In implementation, the pixel resolution is 128×128 , consistent with the simulation. We set the compression ratio as 0.25 and capture approximately 4100 measurements. During imaging process, several factors might influence the final reconstruction. For example, the fluctuation of light source and background light, the instability of detector sensitivity, and minor vibration of the light path. To effectively suppress the imaging noise, we conduct each measurement by averaging over 200 samplings, and maximize the amplification gain of the bucket detector to minimize the detected noise. As can be seen from the Fig. 6, although there still exist a bit artifacts in the reconstruction by introducing the local prior of CSC, the reconstruction of our method perform significant superiority to conventional ones. By additional local prior constraint, the reconstruction of 0.25 compression ratio under experimental condition is decent. The noisy background is suppressed and local details is clearer. For example, the smiling mouth in the image “flower” exhibits clearer edge after CSC introduction; the number “60” of the image “Butterfly” can be obviously resolved in TV+CSC. In sum, through imposing sparse constraints both globally and locally on the SPI framework, the reconstruction quality could be improved significantly.

5. CONCLUSION

In conclusion, this paper propose a high fidelity single-pixel imaging scheme by introducing the local prior of convolutional

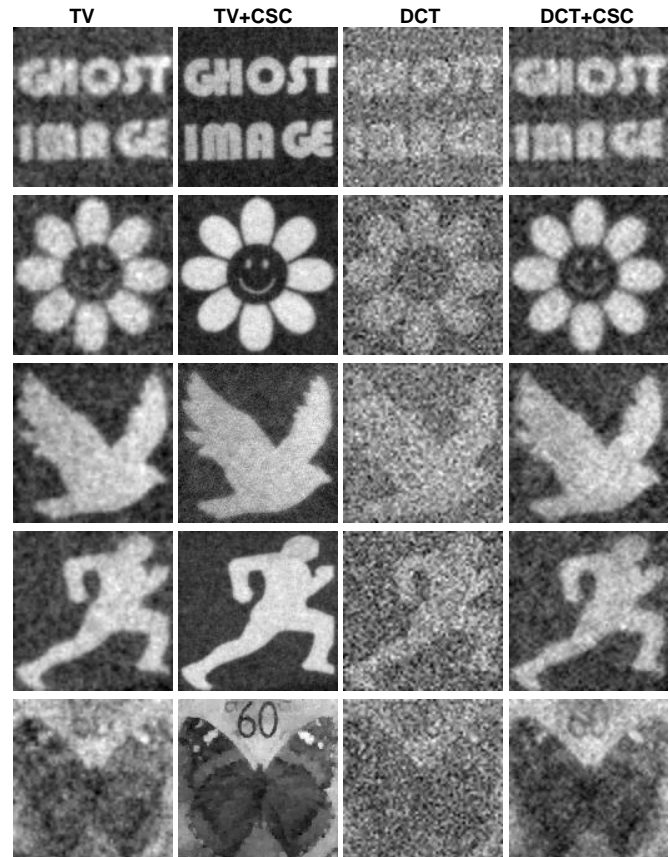


Fig. 6. The reconstruction of the experiment on five different scenes. The compression ratio is 0.25, and each measurement is averaged under 200 samplings.

sparse coding into global prior as TV and DCT. By imposing the combinational constraints on the SPI framework, the reconstruction exhibit significant promotion and thus can decrease the numbers of measurements in practical application. The simulations on the synthetic data tell that the averaged promotion of different compression ratio is approximately 2.5 ~ 6.4 dB in TV and 3.4 ~ 13.7 dB in DCT. Moreover, the experiment also demonstrate the effectiveness of our method.

In terms of computational load, the optimization process of our method would not increase the calculation complexity, compared with conventional compressive sensing based method. The over-complete dictionary can be learned before hand, and the convolutional operator in the optimization could be transformed into frequency domain for matrix multiplication.

Our method can be accomplished without hardware modification based on the conventional SPI scheme. In implementation, considering only 20 natural images is used for training the dictionary, we could obtain higher representative precision through training more natural images or training specific class of natural scenes for the certain target scene. To sum up, our method has the potential to broaden the practical application of single-pixel imaging.

FUNDING INFORMATION

National key foundation for exploring scientific instrument of China (2013YQ140517); National Science Foundation of China (61327902, 61631009).

REFERENCES

1. T. Pittman, Y. Shih, D. Strekalov, and A. Sergienko, "Optical imaging by means of two-photon quantum entanglement," *Phys. Rev. A* **52**, R3429(19995).
2. R. S. Bennink, S. J. Bentley, and R. W. Boyd, "Two-photon coincidence imaging with a classical source," *Phys. Rev. Lett* **89**, 113601 (2002)
3. A. Gatti, E. Brambilla, M. Bache, and L. A. Lugiato, "Ghost imaging with thermal light: comparing entanglement and classical correlation," *Phys. Rev. Lett.* **93**, 093602 (2004).
4. A. Valencia, G. Scarcelli, M. D'Angelo, and Y. Shih, "Two-photon imaging with thermal light," *Phys. Rev. Lett.* **94**, 063601 (2005).
5. N. Tian, Q. Guo, A. Wang, D. Xu, and L. Fu, "Fluorescence ghost imaging with pseudothermal light," *Opt. Lett.* **36**, 3302–3304 (2011).
6. C. Zhao, W. Gong, M. Chen, E. Li, H. Wang, W. Xu, and S. Han, "Ghost imaging lidar via sparsity constraints," *Appl. Phys. Lett.* **101**, 141123 (2012).
7. B. Sun, M. P. Edgar, R. Bowman, L. E. Vittert, S. Welsh, A. Bowman, and M. Padgett, "3D computational imaging with single-pixel detectors," *Science* **340**, 844–847 (2013).
8. P. Clemente, V. Durán, E. Tajahuerce, and J. Lancis, "Optical encryption based on computational ghost imaging," *Opt. Lett.* **35**, 2391–2393 (2010).
9. W. Chen and X. Chen, "Ghost imaging for three-dimensional optical security," *Appl. Phys. Lett.* **103**, 221106 (2013).
10. O. S. Magana-Loaiza, G. A. Howland, M. Malik, J. C. Howell, and R. W. Boyd, "Compressive object tracking using entangled photons," *Appl. Phys. Lett.* **102**, 231104 (2013).
11. E. Li, Z. Bo, M. Chen, W. Gong, and S. Han, "Ghost imaging of a moving target with an unknown constant speed," *Appl. Phys. Lett.* **104**, 251120 (2014).
12. Y. Bromberg, O. Katz, and Y. Silberberg, "Ghost imaging with a single detector," *Phys. Rev. A* **79**, 053840 (2009).
13. W. Gong and S. Han, "A method to improve the visibility of ghost images obtained by thermal light," *Phys. Lett. A* **374**, 1005–1008 (2010).
14. F. Ferri, D. Magatti, L. Lugiato, and A. Gatti, "Differential ghost imaging," *Phys. Rev. Lett.* **104**, 253603 (2010).
15. B. Sun, S. S. Welsh, M. P. Edgar, J. H. Shapiro, and M. J. Padgett, "Normalized ghost imaging," *Opt. Express* **20**, 16892–16901 (2012).
16. K. Guo, S. Jiang, and G. Zheng, "Multilayer fluorescence imaging on a single-pixel detector," *Biomed. Opt. Express* **7**, 2425–2431 (2016).
17. W. Wang, X. Hu, J. Liu, S. Zhang, J. Suo, and G. Situ, "Gerchberg-Saxton-like ghost imaging," *Opt. Express* **23**, 28416 (2015).
18. C. Deng, J. Suo, Y. Wang, Z. Zhang and Q. Dai, "Single-shot thermal ghost imaging using wavelength-division multiplexing," *Appl. Phys. Lett.* **5**, 051107 (2018)
19. O. Katz, Y. Bromberg, and Y. Silberberg, "Compressive ghost imaging," *Appl. Phys. Lett.* **95**, 131110 (2009).
20. M. Aßmann and M. Bayer, "Compressive adaptive computational ghost imaging," *Sci. Rep.* **3**, 1545 (2013).
21. L. Bian, J. Suo, Q. Dai and F. Chen, "Experimental comparison of single-pixel imaging algorithms," *JOSA A* **35**, 78–87 (2018).
22. W. Yu, M. Li, X. Yao, X. Liu, L. Wu, and G. Zhai, "Adaptive compressive ghost imaging based on wavelet trees and sparse representation," *Opt. Express* **22**, 7133–7144 (2014).
23. W. Gong and S. Han, "High-resolution far-field ghost imaging via sparsity constraint," *Sci. Rep.* **5**, 9280 (2015).
24. J. Yang, J. Wright, T. Huang, and Y. M, "Image super-resolution via sparse representation," *IEEE trans. image process.* **19**, 2861–2873 (2010).
25. J. Wright, Y. Ma, J. Mairal, G. Sapiro, T. Huang and S. Yan, "Sparse representation for computer vision and pattern recognition," in *Proceedings of the IEEE* (IEEE, 2010), pp. 1031–1044.
26. C. Bao, H. Ji, Y. Quan and Z. Shen, "Dictionary learning for sparse coding: Algorithms and convergence analysis," *IEEE Trans. Pattern Anal. Mach. Intell.* **38**, 1356–1369 (2016).
27. X. Hu, J. Suo, T. Yue, L. Bian and Q. Dai, "Patch-primitive driven compressive ghost imaging," *Opt. Express* **23**, 11092–111042 (2015).
28. S. Gu, W. Zuo, Q. Xie, D. Meng, X. Feng, and L. Zhang, "Convolutional sparse coding for image super-resolution", in *Proceedings of the IEEE Conference on Computer Vision* (IEEE, 2015), pp. 1823–1831.
29. H. Bristow, A. Eriksson, and S. Lucey, "Fast convolutional sparse coding," in *Proceedings of the IEEE Conference on Computer Vision and Pattern Recognition* (IEEE, 2013), pp. 391–398.
30. F. Heide, W. Heidrich, and G. Wetzstein, "Fast and flexible convolutional sparse coding," in *Proceedings of the IEEE Conference on Computer Vision and Pattern Recognition* (IEEE, 2015), pp. 5135–5143.
31. S. Boyd, N. Parikh, E. Chu, B. Peleato, and J. Eckstein, "Distributed optimization and statistical learning via the alternating direction method of multipliers," *Found. Trends Mach. Learn.* **3**, 1–122 (2011).
32. O. Russakovsky, J. Deng, H. Su, J. Krause, S. Satheesh, S. Ma, Z. Huang, A. Karpathy, A. Khosla, M. Bernstein, A. C. Berg and F. Li, "Imagenet large scale visual recognition challenge," *Int. J. Comput. Vis.* **115**, 211–252 (2015)